Electronic Supplementary Information (ESI) for Energy & Environmental Science.
This journal is © The Royal Society of Chemistry 2017

Supporting Information

Interface passivation using ultrathin polymer-fullerene films for high-efficiency perovskite solar cells with negligible hysteresis

Jun Peng,*[a] Yiliang Wu,[a] Wang Ye,[b] Daniel A. Jacobs,[a] Heping Shen,[a] Xiao Fu,[a] Yimao Wan,[a] The Duong,[a] Nandi Wu,[a] Chog Barugkin,[a] Hieu T. Nguyen,[a] Dingyong Zhong,[b] Juntao Li,[b] Teng Lu,[c] Yun Liu,[c] Mark N. Lockrey,[d] Klaus J. Weber,[a] Kylie R. Catchpole,[a] Thomas P. White*[ab]

[a]*Research School of Engineering, The Australian National University, Canberra, ACT, 2601, Australia*
[b]*State Key Laboratory of Optoelectronic Materials and Technologies, School of Physics, Sun Yat-sen University, Guangzhou 510275, China*
[c]*Research School of Chemistry, The Australian National University, Canberra, ACT, 2601, Australia*
[d]*Australian National Fabrication Facility, Department of Electronic Materials Engineering, Research School of Physics & Engineering, The Australian National University, Canberra, ACT, 2601, Australia*

E-mail: u5686151@anu.edu.au; or pengjun.88.81@gmail.com
thomas.white@anu.edu.au

Experimental Section

Precursor solution preparation

In-TiO_x precursor solution. The In-TiO_x precursor solution was prepared as described in our previous work.[1]

PMMA and PCBM precursor solution. PMMA precursor solution was prepared by dissolving 1 mg/mL PMMA (Sigma Aldrich, MW~120,000) in Chlorobenzene. PCBM precursor

solution was prepared by dissolving 5 mg/mL PCBM (Sigma Aldrich, 99.0%) in Chlorobenzene.

PMMA:PCBM precursor solution. PMMA:PCBM (1:1) precursor solution was prepared by dissolving 1 mg PMMA, and 1 mg PCBM into 1 mL Chlorobenzene. PMMA:PCBM (1:3) precursor solution was prepared by dissolving 1 mg PMMA, and 3 mg PCBM into 1 mL Chlorobenzene. PMMA:PCBM (1:5) precursor solution was prepared by dissolving 1 mg PMMA, and 5 mg PCBM into 1 mL Chlorobenzene.

Mixed-cation perovskite precursor solution. The $Cs_{0.07}Rb_{0.03}FA_{0.765}MA_{0.135}PbI_{2.55}Br_{0.45}$ perovskite precursor solution contains 1.2 M lead iodide (PbI_2, 99%, Sigma Aldrich), 1.1 M formamidinium (FAI, Dyesol), 0.2 M lead bromide ($PbBr_2$, 99.999%, Sigma Aldrich), 0.2 M methylamine bromide (MABr, Dyesol), 0.091 M cesium iodide (CsI, 99.999%, Sigma Aldrich), and 0.039 M rubidium iodide (RbI, 99.9%, Sigma Aldrich) in 1 mL anhydrous DMF:DMSO (4:1, v/v, Sigma Aldrich).

Spiro-OMeTAD precursor solution. Spiro-OMeTAD precursor solution was prepared by dissolving 72.5 mg Spiro-OMeTAD, 28.5 µL 4-tert-butylpyridine and 17.5 µL of lithium bis(trifluoromethanesulfonyl)imide solution (520mg/mL in acetonitrile) in 1 mL Chlorobenzene. Note that after spin-coating the Spiro-OMeTAD solution, the substrates are placed in air in a humidity-control box for 12 hours to ensure sufficient oxidation of the Spiro-OMeTAD film prior to electrode/contact layer deposition.

Device fabrication and *J-V* characterization

Device fabrication. ~70 nm In-TiO_x compact layers, and ~110 nm mesoporous TiO_2 (30 NR-D, Dyesol) were sequentially deposited on the pre-cleaned FTO (7Ω/□, Dyesol) substrates according to Ref. [1]. For the ultra-thin passivation layer deposition, 30 µL PMMA, PMMA:PCBM, and PCBM precursor solution were dropped on the top of the FTO/*c*-In-TiO_x/*m*-TiO_2 substrates and separately deposited by spin-coating at 5000 rpm/s with a ramp of 5000 rpm s^{-1} for 30 s, then annealed at 100 ^oC for 10 min. Then, $Cs_{0.07}Rb_{0.03}FA_{0.765}MA_{0.135}PbI_{2.55}Br_{0.45}$ thin film was deposited by a two-step spin coating program: first at 2000 rpm with a ramp of 200 rpm s^{-1} for 10 s, and then at 4000 rpm with a ramp of 1000 rpm s^{-1} for 20 s. During the second step, around 100 µl Chlorobenzene was poured on the spinning substrates 5 s prior to the end of the program. Substrates were then

annealed at 100 °C for 45 min. Then, Spiro-OMeTAD thin film was deposited via spin coating at 3000 rpm with a ramp of 3000 rpm s^{-1} for 30 s. Finally, ~100 nm gold was deposited through a shadow mask (cell's effective area, 0.16 cm^2). Note that all depositions were conducted in a nitrogen-filled glovebox.

J-V measurement. All devices were tested under 1 sun conditions (100 mW/cm^2, AM 1.5G, 25 °C) in a solar simulator system (model #SS150 from Photo Emission Tech Inc) equipped with a Xenon lamp. The light intensity was calibrated using a certified Fraunhofer CalLab reference cell. For the perovskite solar cells, all cells' *J-V* curves were tested at a 50 mV/s scan rate in a custom-built vacuum measurement jig without aperture mask. Note that reverse scan is from V_{oc} to J_{sc} (forward bias → short circuit, 1.2 V → -0.1V), and forward scan is from J_{sc} to V_{oc} (short circuit → forward bias, -0.1 V → 1.2 V). No preconditioning protocol has been used before the characterization.

EQE measurement. The EQE spectra of our perovskite cells were measured with a modified Protoflex QE1400 system without light bias in DC mode using a tungsten light source, two Keithley 2425 sourcemeters, and a reference cell. The EQE response was calibrated using a certified Fraunhofer CalLab reference cell.

Characterization

XPS and UPS. X-ray photoelectron spectroscopy (XPS) and ultraviolet photoelectron spectroscopy (UPS) measurements were carried out on an XPS machine (Escalab 250 Xi, Thermo Fisher), with a monochromatic Al K_α (1486.7 eV) X-ray source for XPS and a He I (21.2 eV) gas discharge lamp for UPS.

SEM. A FEI Verios scanning electron microscope (SEM) was used to investigate the surface morphology of samples. A Helios Nanolab 600 FIB system was used to prepare cross-sectional SEM images of the cells. Energy dispersive X-ray (EDX) (beam conditions: 10 kV, 1.6 nA) and Backscattered electron (BSE) imaging (beam condition: 5 kV, 50 pA) were performed to analyze perovskite materials. Note that ~2 μm Pt used as a protection layer was deposited on sample before preparing the cross-sectional SEM image.

Transmittance. A PerkinElmer Lambda 1050 UV/Vis/NIR spectrophotometer was used to measure the transmittance of the samples.

XRD. X-ray diffraction analysis was performed with a Bruker D2 Phaser diffractometer operated at 30 kV, 10 mA at 2θ (Cu Kα) 10–80°, step 0.02° and scan speed 2.3° min^{-1}.

C-AFM: Conductive atomic force microscopy (C-AFM) measurements were performed on ITO/PMMA and ITO/PMMA:PCBM using Asylum Research Cypher system, where ITO substrates were used as bottom electrodes. Pt/Ir coated conductive tips with spring constant of ~2 N/m and resonant frequencies of ~70 kHz (Asylum research AC240TM) were used for both morphology measurement and C-AFM measurement. Voltages (5 V) were applied between the ITO substrate and the conductive probe tip, and the current was traced by internal preamplifier (Asylum ORCA module, 1 nA/V). As some samples were highly conductive, a 500 MΩ resistance was added to keep the ORCA amplifier from saturating. Note that the ITO/PMMA sample was prepared by spin-coating 2 mg/mL PMMA in CB on pre-cleaned ITO substrate at 2000 rpm/s for 30 s; and the ITO/PMMA:PCBM sample was prepared by spin-coating 4 mg/mL PMMA:PCBM (1:3, w/w) in CB on the pre-cleaned ITO substrate at 2000 rpm/s for 30 s.

Profile AFM. Profile atomic force microscopy (AFM) measurement was performed on Si/*c*-In-TiO_x/PMMA:PCBM sample to estimate the thickness of ultrathin PMMA:PCBM film. In order to reduce the uncertainty, the thin PMMA:PCBM film for profile-AFM measurement was deposited by spin-coating 4 mg/mL PMMA:PCBM (1:3, w/w) in CB at 2000 rpm with a ramp of 2000 rpm/s for 30 s on the top of Si/*c*-In-TiO_x substrate. PMMA and PCBM are organic materials and the blend films are very soft. We therefore used a very sharp blade to create a profile on the top of the Si/*c*-In-TiO_x/PMMA:PCBM sample by softly and gently cutting the surface. Note that we chose polished silicon wafer as substrate, the compact In-TiO_x layer was deposited from exactly the same deposition procedures as described in device fabrication.

PL imaging. For photoluminescence (PL) imaging, the cells were held in a nitrogen-filled and temperature controlled jig. The jig is mounted in a home-built PL imaging system and uniformly illuminated with two 430 nm royal-blue LED chips, filtered by bandpass filters (451/106 nm). Following illumination (Intensity~100 mW/cm^2), a Peltier-cooled (−70 °C) Si CCD camera (Princeton Instruments Pixis 1024) with a long-pass filter (750 nm) took the image of the luminescence from the perovskite cells with the exposure time of 0.2 second. PL images were taken when cells were under both open circuit and reverse bias (-2 V) conditions. The open circuit images were then subtracted from the reverse bias image to ensure the

luminescence emission was solely from the perovskite absorbers as described in our previous work.[2]

TRPL. Time-resolved photoluminescence (TRPL) decay measurements were performed using a LabRAM HR Evolution system with a time-correlated single photon counting (TCSPC) system (DeltaPro-DD, Horiba). A 508nm diode laser (DD-510L, Horiba) with pulse duration of 110ps, fluence of ~10 μJ/cm^2/pulse, and a repetition rate of 312.5 kHz was used for excitation. The PL signal was extracted at 770 nm. Both the incident light and the reflected light went through a 50x objective lens (LEICA PL FLUOTAR L 50/0.55), which resulted in a spot size of ~2 μm. The samples were kept in N_2 environment during the measurements. For the analysis of the time-resolved PL decay, a bi-exponential model in the Decay Analysis software was used to fit the experimental result and extract the lifetime.

SCLC. Space charge limited current (SCLC) measurements were performed on electron-dominated devices with a structure of FTO/c-In-TiO_x/m-TiO_2/(with or without PMMA:PCBM passivation layer)/Mixed-cation Perovskite/PCBM (~50 nm)/Ag (~100 nm), where the device without PMMA:PCBM layer is the control device (non-passivated cell), and the device with PMMA:PCBM layer is the passivated device. Note that the electron-dominated devices were prepared by the same procedures as described in the aforementioned device fabrication Then, ~ 50 nm PCBM was deposited by spin-coating 20 mg/mL PCBM in CB at 1000 rpm/s for 40 s; and then, ~100 nm Ag was deposited by thermal evaporation at a deposition rate of 1 Å/s. All SCLC tests were carried out at room temperature and under dark.

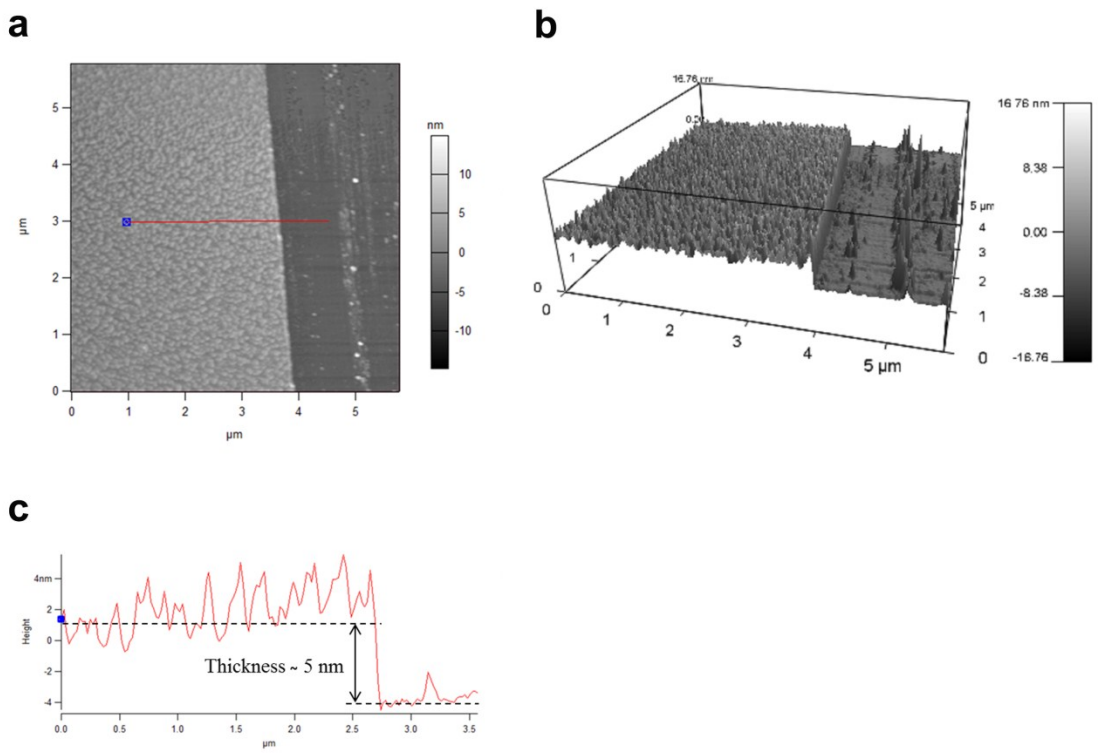

Fig. S1 a) 2-D AFM image of 5 µm × 5 µm region of Si/*c*-In-TiO_x/PMMA:PCBM. b) 3-D AFM image of 5 µm × 5 µm region of Si/*c*-In-TiO_x/PMMA:PCBM. c) The corresponding line profiling analysis of PMMA:PCBM-coated on Si/*c*-In-TiO_x substrate. Note that the PMMA:PCBM layer for profile-AFM measurement was deposited by spin-coating 4 mg/mL PMMA:PCBM (1:3, w/w) in CB at 2000 rpm with a ramp of 2000 rpm/s for 30 s on the top of Si/*c*-In-TiO_x substrate.

Fig. S1 shows the thickness of PMMA:PCBM film on the Si/*c*-In-TiOx/PMMA:PCBM sample is around 5 nm. As the thin PMMA:PCBM film used as a passivation layer in our passivated perovskite cell was deposited by spin-coating 4 mg/mL PMMA:PCBM (1:3, w/w) in CB at 5000 rpm with a ramp of 5000 rpm/s for 30 s, the estimated thickness of PMMA:PCBM passivation layer in our passivated cell was less than 5 nm.

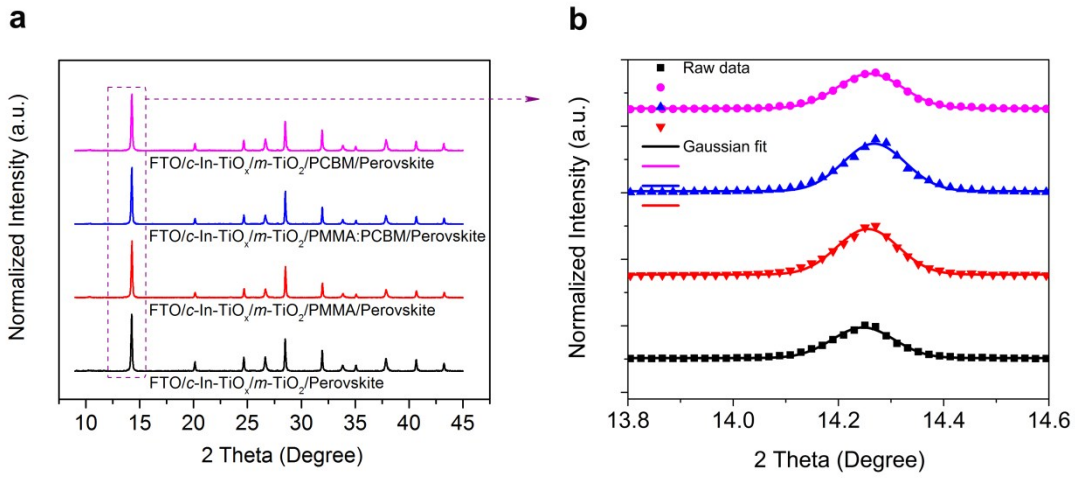

Fig. S2 a) XRD spectra of the perovskite thin films deposited on different FTO/*c*-In-TiO_x/m-TiO_2 substrates with/without the PMMA, PMMA:PCBM or PCBM passivation layer. b) The corresponding Gaussian fit of the dominant black perovskite phase for perovskite thin film. Note that the perovskite composition is $Cs_{0.07}Rb_{0.03}FA_{0.765}MA_{0.135}PbI_{2.55}Br_{0.45}$.

In Fig. S2a, the XRD spectra show no systematic variations with substrates, and no obvious PbI_2 or other non-perovskite phases. To further investigate the crystallite size of perovskite, the dominant black perovskite phase is fitted with a Gaussian distribution to determine the full width at half maximum (FWHM) for each sample. As shown in the Fig. S2b, it reveals that the value of FWHM for FTO/*c*-In-TiO_x/*m*-TiO_2/perovskite sample is 0.13915, while the values of FWHM for the perovskite thin films deposited on different FTO/c-In-TiO_x/m-TiO_2 substrates with an ultrathin PMMA, PMMA:PCBM or PCBM passivation layer are 0.13788, 0.13931 or 0.1466, respectively. The calculated FWHM shows that there are no significant variations for the crystallite size of perovskite with different substrates.

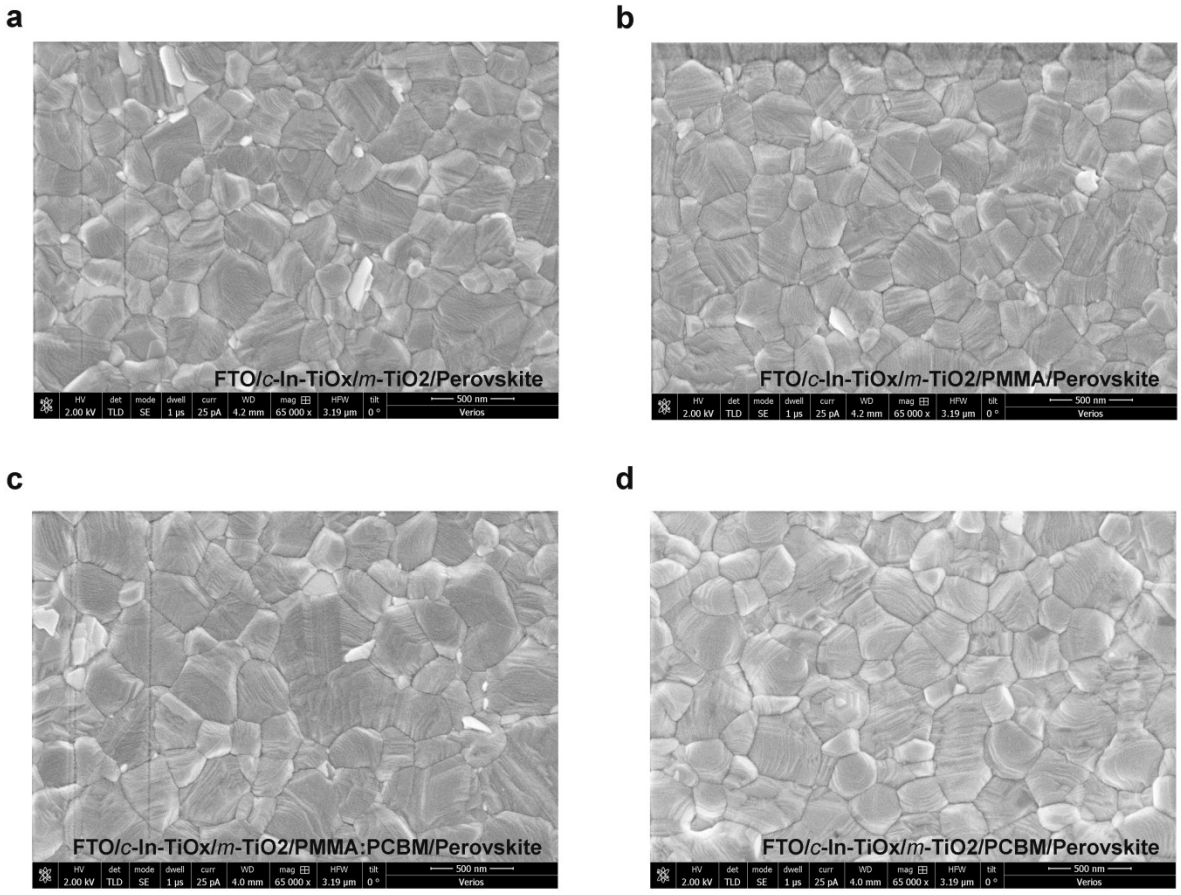

Fig. S3 SEM images of perovskite films deposited on different substrates: a) FTO/*c*-In-TiO_x/*m*-TiO_2. b) FTO/*c*-In-TiO_x/*m*-TiO_2/PMMA. c) FTO/*c*-In-TiO_x/*m*-TiO_2/PMMA:PCBM. d) FTO/*c*-In-TiO_x/*m*-TiO_2/PCBM. Note that the perovskite composition is $Cs_{0.07}Rb_{0.03}FA_{0.765}MA_{0.135}PbI_{2.55}Br_{0.45}$; the ratio of PMMA:PCBM is 1:3 (w/w).

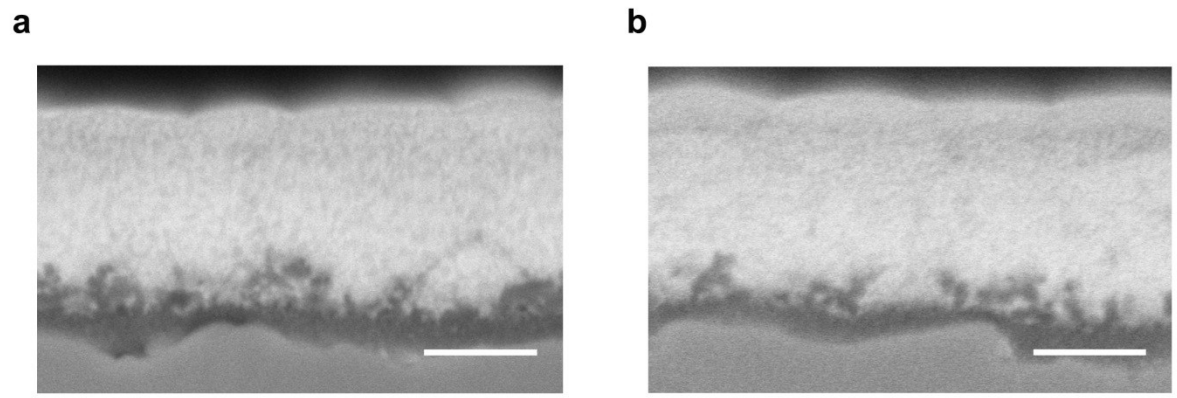

Fig. S4 SEM backscattered electron (BSE) imaging measurements. a) FTO/*c*-In-TiO_x/*m*-TiO_2/Perovskite/Spiro-OMeTAD/Au. b) FTO/*c*-In-TiO_x/*m*-TiO_2/ PMMA:PCBM/Perovskite /Spiro-OMeTAD/Au. Note that the perovskite composition is $Cs_{0.07}Rb_{0.03}FA_{0.765}MA_{0.135}PbI_{2.55}Br_{0.45}$.

Backscattered electron (BSE) imaging has been used to investigate the penetration of the perovskite into the mesoporous TiO_2 region for cross-sections of both non-passivated and passivated cells (with a PMMA:PCBM passivation layer). The contrast in BSE images is proportional to the average atomic number. This allows for discrimination between areas of different material composition. From the BSE image we can clearly see the difference between the perovskite (bright), *m*-TiO_2 and compact In-TiO_x (dark), and SnO_2 (medium) (see Fig. S4). From Fig. S4 we can see that the mesoporous TiO_2 extends into the perovskite layer and the perovskite fully penetrates into this layer leaving no voids.

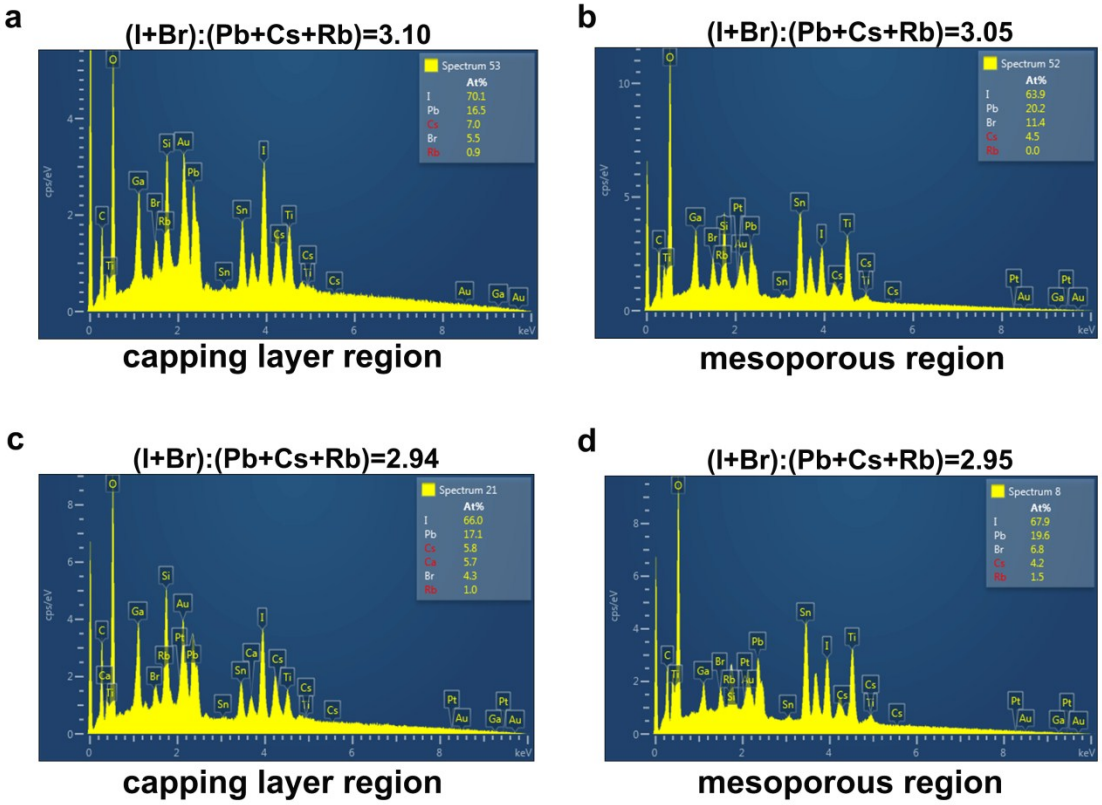

Fig. S5 SEM energy dispersive X-ray detector (EDX) measurements. a) EDX measurement on the perovskite capping layer region and b) EDX measurement on the mesoporous TiO2 region for FTO/*c*-In-TiO_x/*m*-TiO_2/ Perovskite/Spiro-OMeTAD/Au (non-passivated cell); c) EDX measurement on the perovskite capping layer region and d) EDX measurement on the mesoporous TiO2 region for FTO/*c*-In-TiO_x/*m*-TiO_2/PMMA:PCBM/Perovskite/Spiro-OMeTAD/Au (passivated cell). Note that the perovskite composition is $Cs_{0.07}Rb_{0.03}FA_{0.765}MA_{0.135}PbI_{2.55}Br_{0.45}$.

In addition, SEM energy dispersive X-ray (EDX) analysis was performed on the mesoporous TiO_2 and perovskite capping layer areas for cross-sections of both non-passivated and passivated cells using an electron beam voltage of 10 kV. From the ratio of (I+Br) to (Pb+Cs+Rb), it can be seen that the composition between the mesoporous TiO_2 region-perovskite capping layer region and across the samples remains close to 3:1 (see Fig. S5).

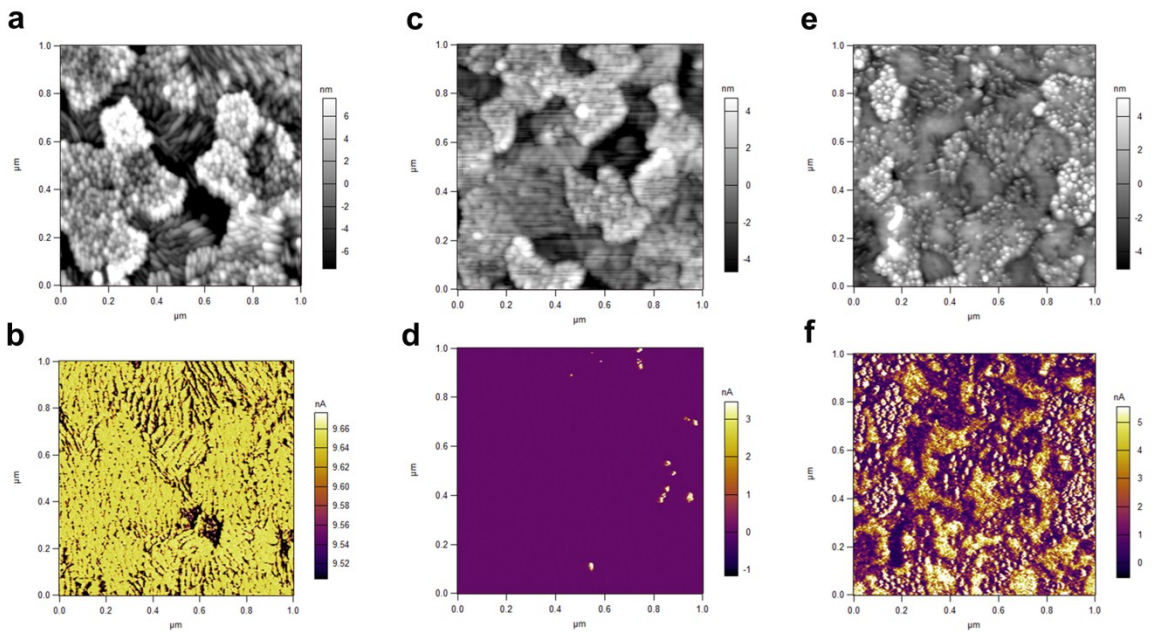

Fig. S6 2-D atomic force microscopy (AFM) images, image scale: 1 µm × 1 µm. a) Surface morphology of Glass/ITO. b) Current mapping of Glass/ITO. c) Surface morphology of Glass/ITO/PMMA. d) Current mapping of Glass/ITO/PMMA. e) Surface morphology of Glass/ITO/PMMA:PCBM. f) Current mapping of Glass/ITO/PMMA:PCBM.

Fig. S6a shows the surface morphology for ITO, where the bright and dark contrast suggests the protrusions and depressions and the maximum height difference is around 15 nm. It reveals that the surface of bare ITO substrate is relatively smooth with root mean square roughness of ~ 3.8 nm. Fig. S6b is the current mapping of the same area for the bare ITO substrate. It is evident that the whole region presents relatively homogeneous current around 9.6 nA, consistent with conductivity of ITO. (Note that in order to avoid current saturation, a 500 MΩ resistor was connected in series, and therefore the 5 V bias on the sample will induce a maximum current of around 10 nA). When a PMMA thin film is present on the ITO substrate, it is obvious that the height contrast decreases in comparison with that observed for the bare ITO substrate (see Fig. S6c). The distribution of the current is quite homogeneous and negligible (with most areas ~ 30 pA), indicating the insulating behavior of the PMMA (see Fig. S6d). Although most of the area for Glass/ITO/PMMA sample behaves as insulating, some points exhibit strong currents which possibly results from pinholes in the film. For the PMMA:PCBM composite thin film on an ITO substrate, the surface is more smooth compared to the bare ITO substrate (see Fig. S6e). The current distribution is inhomogeneous, which is different from the conductive ITO and insulating PMMA (see Fig. S6f). The results demonstrate the conductive characteristics of PMMA:PCBM, with some regions with yellow

color (~4 nA) presenting good conductive properties, while others with violet color (≤1 nA) show higher resistance. This clearly confirms the role of PCBM as an additive increasing the conductivity of PMMA:PCBM blend films.

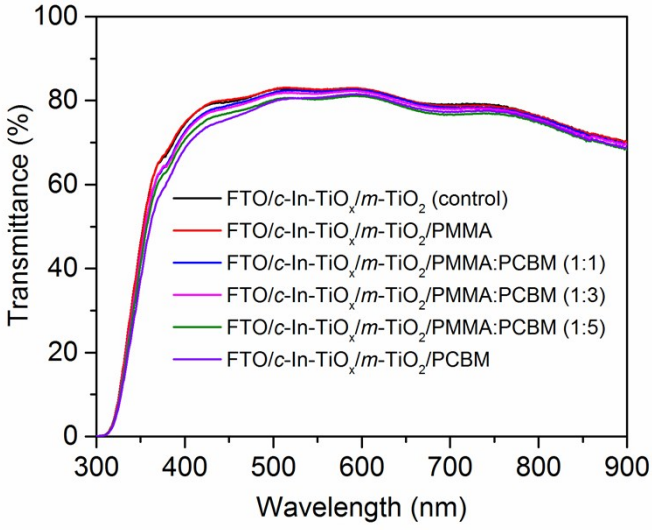

Fig. S7 Transmittance spectra of the FTO/*c*-In-TiO_x/*m*-TiO_2 substrates with/without the PMMA, PMMA:PCBM, or PCBM passivation layer.

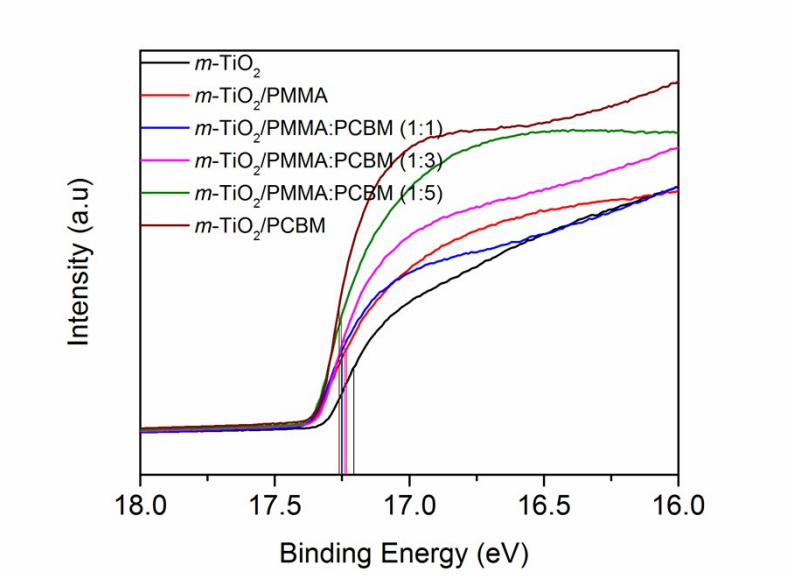

Fig. S8 UPS spectra of FTO/*c*-In-TiO_x/*m*-TiO_2 (labeled as *m*-TiO_2), FTO/*c*-In-TiO_x/*m*-TiO_2/PMMA (labeled as *m*-TiO_2/PMMA), FTO/*c*-In-TiO_x/*m*-TiO_2/PMMA:PCBM (labeled as *m*-TiO_2/PMMA:PCBM) and FTO/*c*-In-TiO_x/*m*-TiO_2/PCBM (labeled as *m*-TiO_2/PCBM). Note that the PMMA:PCBM (1:1) represents the ratio of PMMA:PCBM is 1:1 (w/w); the PMMA:PCBM (1:3) represents the ratio of PMMA:PCBM is 1:3 (w/w); the PMMA:PCBM (1:5) represents the ratio of PMMA:PCBM is 1:5 (w/w).

As shown in Fig. S8, the photoemission cutoff is determined by the UPS measurement,[3] the obtained work function (WF) of FTO/*c*-In-TiO_x/m-TiO_2 is ~ 4.0 eV. The WF of FTO/*c*-In-TiO_x/*m*-TiO_2/PMMA is ~3.97 eV, which is slightly lower than that of the FTO/*c*-In-TiO_x/m-TiO_2. In addition, the WF of FTO/*c*-In-TiO_x/*m*-TiO_2/PMMA:PCBM (1:1) and FTO/*c*-In-TiO_x/*m*-TiO_2/PMMA:PCBM (1:3) are ~3.95 eV and ~3.96 eV, respectively. Similarly, the WF of FTO/*c*-In-TiO_x/*m*-TiO_2/PMMA:PCBM (1:5) is ~3.95 eV. Note that the WF values of these samples with different ratios of the PMMA:PCBM passivation layers show no significant difference. To reveal the effect of the PCBM material, the sample with pure PCBM passivation layer was also investigated and shows that the WF of FTO/*c*-In-TiO_x/*m*-TiO_2/PCBM is ~3.94 eV.

Based on the aforementioned UPS analysis, we found that the WF of FTO/*c*-In-TiO_x/*m*-TiO_2/PMMA (~3.97 eV) shows 30 meV difference as compared to FTO/*c*-In-TiO_x/*m*-TiO_2 (~4.0 eV); the WF of FTO/*c*-In-TiO_x/*m*-TiO_2/PMMA:PCBM with different ratios of PMMA:PCBM show 40 meV - 50 meV variations as compared to FTO/*c*-In-TiO_x/*m*-TiO_2; moreover, the WF of FTO/*c*-In-TiO_x/*m*-TiO_2/PCBM (~3.94 eV) shows 60 meV difference as compared to FTO/*c*-In-TiO_x/*m*-TiO_2 (~4.0 eV).

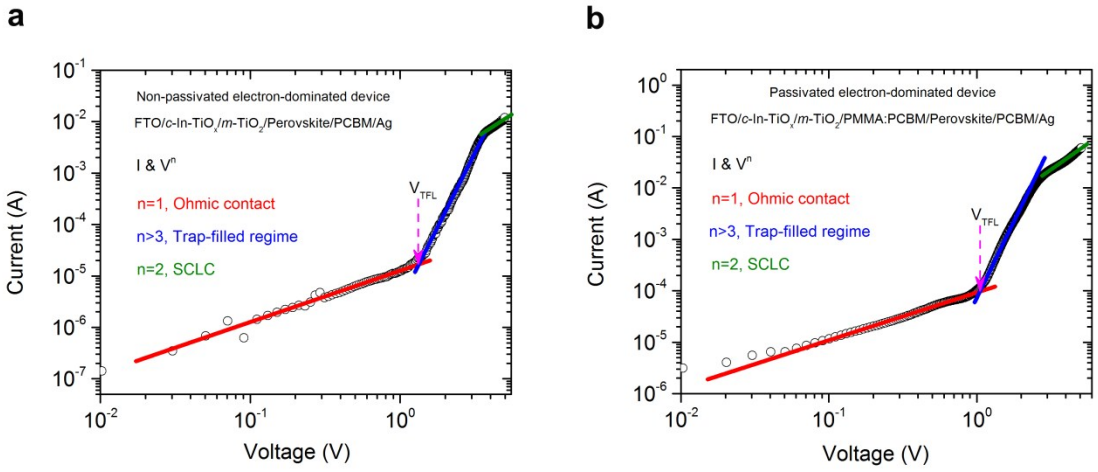

Fig. S9 Space charge limited current (SCLC) measurements. a) Non-passivated electron-dominated device with a structure of FTO/*c*-In-TiO_x/*m*-TiO_2/Perovskite/PCBM/Ag. b) Passivated electron-dominated device with a structure of FTO/*c*-In-TiO_x/*m*-TiO_2/PMMA:PCBM/Perovskite/PCBM/Ag. Note that the perovskite composition is $Cs_{0.07}Rb_{0.03}FA_{0.765}MA_{0.135}PbI_{2.55}Br_{0.45}$.

To further investigate the density of defects or trap states within our passivated and non-passivated perovskite cells, space charge limited current (SCLC) measurements were performed on both non-passivated and passivated electron-dominated devices, where the device structure is: FTO/*c*-In-TiO_x/*m*-TiO_2/(w/wo PMMA:PCBM)/Perovskite/PCBM/Ag. As shown in the Fig. S9, three regions (ohmic contact regime, trap-filled regime and SCLC regime) were evident in the logarithmic plot of the *I-V* characteristics of the non-passivated and passivated electron-dominated devices.[4,5] In the SCLC model, the density of defects or trap states can be simply and roughly estimated by the onset voltage V_{TFL} (trap-filled limit (TFL) a regime in which all available defects or trap states were filled by the injected carries) based on the equation of $V_{TFL}=(e*n_t*d^2)/(2*\varepsilon*\varepsilon_0)$, where e, n_t, d, ε and ε_0 are electronic charge, trap density, the thickness of device, the dielectric constant of perovskite material and the permittivity of free space, respectively.[5] For the passivated electron-dominated device, the V_{TFL} was of 1.06 V, while the V_{TFL} for the non-passivated device was 1.32 V shown in the Fig. S9. Based on the V_{TFL} equation, we found that the trap density for our passivated device was lower than that of the non-passivated device. Hence, the evidence from space charge limited current (SCLC) measurements for our passivated and non-passivated cells may further support our findings obtained from the steady-state PL and transient PL measurements.

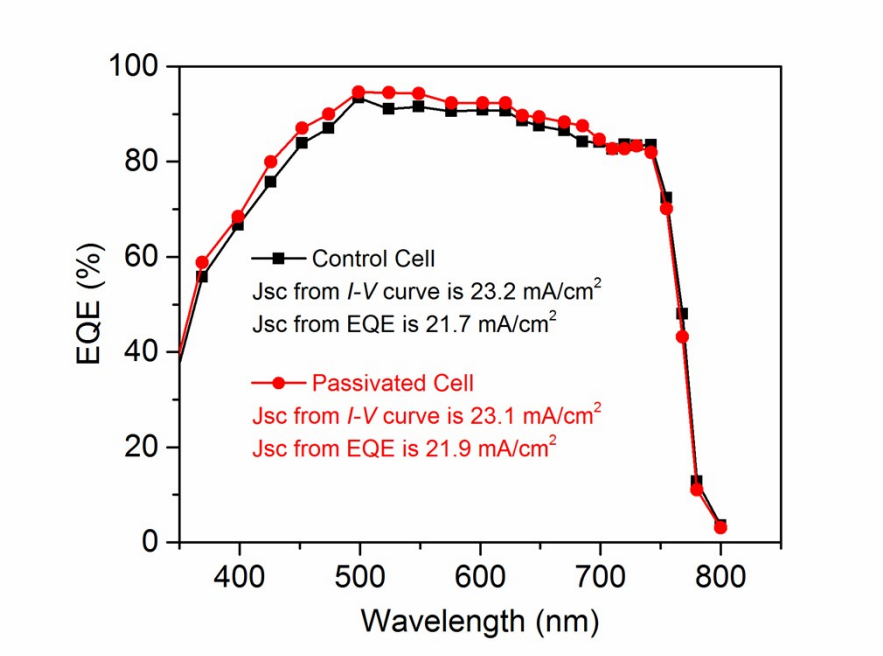

Fig. S10 EQE spectra of the control cell and passivated cell.

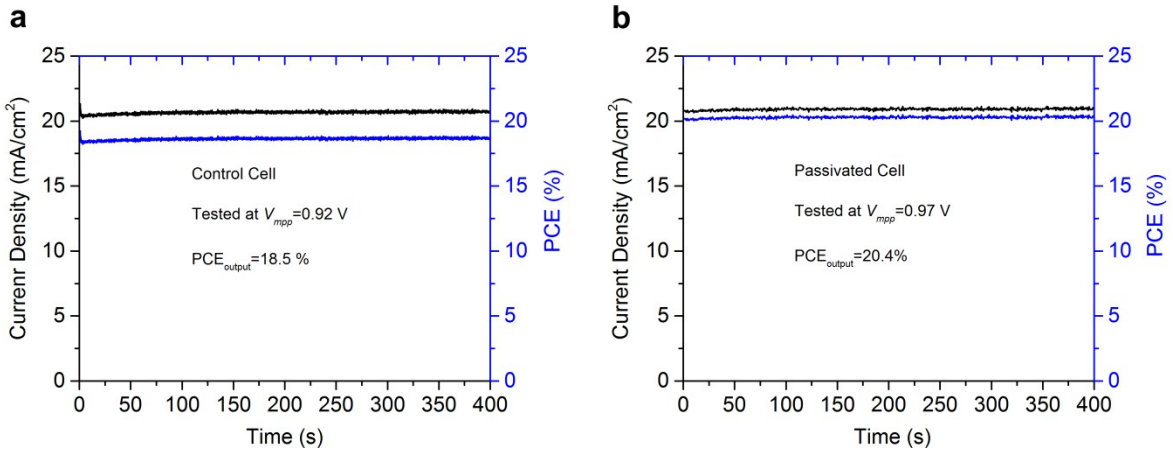

Fig. S11 a) Steady-state PCE of the control cell with a structure of FTO/*c*-In-TiO_x/*m*-TiO_2/Perovskite/Spiro/Au tested at the V_{mpp} of 0.92 V. b) The steady-state PCE of the passivated cell with a structure of FTO/*c*-In-TiO_x/*m*-TiO_2/PMMA:PCBM (1:3)/Perovskite/Spiro/Au tested at the V_{mpp} of 0.97 V.

Table S1 Photovoltaic parameters of the control cell with a structure of FTO/*c*-In-TiO_x/*m*-TiO_2/Perovskite/Spiro/Au.

Scan rates [mV/s]	Scan direction	V_{oc} [V]	J_{sc} [mA/cm^2]	FF [%]	PCE [%]	$\Delta_{(PCE)}$=$RS_{(PCE)}$-$FS_{(PCE)}$ [%]
500	RS	1.10	23.12	78.5	19.96	2.15
	FS	1.075	23.01	72.0	17.81	
200	RS	1.09	23.12	77.9	19.62	1.96
	FS	1.07	23.12	71.4	17.66	
50	RS	1.09	23.20	77.5	19.60	0.90
	FS	1.10	23.30	72.8	18.70	
1	RS	1.10	23.15	73.6	18.74	1.00
	FS	1.10	23.20	69.5	17.74	

Note that the perovskite stands for $Cs_{0.07}Rb_{0.03}FA_{0.765}MA_{0.135}PbI_{2.55}Br_{0.45}$; the legend of RS represents reverse scan (from V_{oc} to J_{sc}), FS represents forward scan (from J_{sc} to V_{oc}).

Table S2 Photovoltaic parameters of the passivated cell with a structure of FTO/*c*-In-TiO_x/*m*-TiO_2/PMMA:PCBM (1:3)/Perovskite/Spiro/Au.

Scan rates [mV/s]	Scan direction	V_{oc} [V]	J_{sc} [mA/cm^2]	FF [%]	PCE [%]	$\Delta_{(PCE)}$=$RS_{(PCE)}$-$FS_{(PCE)}$ [%]
500	RS	1.155	23.10	76.8	20.49	0.52
	FS	1.145	23.22	75.1	19.97	
200	RS	1.165	23.09	76.0	20.43	0.32
	FS	1.155	23.15	75.2	20.11	
50	RS	1.160	23.10	76.2	20.40	0
	FS	1.160	23.20	76.0	20.40	
1	RS	1.155	23.05	74.9	19.94	0.36
	FS	1.155	23.15	73.2	19.58	

RS represents reverse scan (from V_{oc} to J_{sc}), FS represents forward scan (from J_{sc} to V_{oc}).

Table S3 Summary of photovoltaic parameters for the n-i-p perovskite solar cells reported with over 20% efficiency.

ETLs	Scan rates [mV/s]	Scan direction	V_{oc} [V]	J_{sc} [mA/cm^2]	FF [%]	PCE [%]	$\Delta_{(PCE)}$=RS$_{(PCE)}$-FS$_{(PCE)}$ [%]	Reference
m-TiO_2 /PMMA:PCBM	50	RS	**1.16**	23.10	76.2	20.4	0	This work
		FS	**1.16**	23.20	76.0	20.4		
m-TiO_2	6	RS	1.117	23.72	77.9	20.6	0.4	6
		FS	1.11	23.67	76.8	20.2		
m-TiO_2	250	RS	1.06	24.70	77.5	20.2	0	7
		FS	1.06	24.70	77.5	20.2		
Cl-capped TiO_2	50	RS	**1.189**	22.30	80.6	21.4	0	8
		FS	**1.189**	22.30	80.6	21.4		
La-doped $BaSnO_3$	250	RS	1.12	23.40	81.3	21.3	n/a	9
		FS	n/a	n/a	n/a	n/a		
Li-doped *m*-TiO_2	10	RS	**1.18**	22.80	81.0	21.8	0.5	10
		FS	**1.173**	22.80	80.0	21.3		
m-TiO_2	50	RS	1.141	23.19	75.7	20.38	0.23	11
		FS	1.145	23.28	76.0	20.61		
SnO_2	n/a	RS	1.09	24.87	74.7	20.27	0.27	12
		FS	1.09	24.88	75.7	20.54		
m-TiO_2	10	RS	**1.167**	23.20	73.6	20.0	0.2	13
		FS	**1.17**	23.3	72.7	19.8		
SnO_2	10	RS	**1.18**	22.37	77.0	20.46	n/a	14
		FS	**n/a**	n/a	n/a	n/a		
m-TiO_2/Au@SiO_2	n/a	RS	**1.16**	23.8	0.74	20.6	0.3	15
		FS	**1.16**	23.8	0.73	20.3		
m-TiO_2	10	RS	**1.16**	24.6	73.0	20.8	0	16
		FS	**1.16**	24.6	73.00	20.8		
m-TiO_2	23.7	RS	1.09	23.43	79.97	20.44	1.93	17
		FS	1.09	23.06	73.78	18.51		
C_{60}:PhIm/C_{60}	n/a	RS	1.141	22.08	80.5	20.3	n/a	18
		FS	n/a	n/a	n/a	n/a		
m-TiO_2	10	RS	1.13	23.7	77.0	21.3	0.3	19
		FS	1.14	23.7	0.78	21.6		
Li-doped *m*-TiO_2	10	RS	**1.147**	23.5	78.5	21.17	0.85	20
		FS	**1.158**	23.5	74.6	20.32		

--- continue ---

In-doped TiO_x	50	RS	1.10	23.1	79.1	20.1	1.4	1
		FS	1.09	23.2	74.0	18.7		
TiO_2:TOPD/PCBM	n/a	RS	1.1	23.2	80.0	20.3	0.5	21
	n/a	FS	1.09	23.2	79.0	19.8		

References

1 J. Peng, T. Duong, X. Z. Zhou, H. P. Shen, Y. L. Wu, H. K. Mulmudi, Y. M. Wan, D. Y. Zhong, J. T. Li, T. Tsuzuki, K. J. Weber, K. R. Catchpole and T. P. White, *Adv. Energy Mater.*, 2017, **7**, 1601768.

2 Y. Wu, H. Shen, D. Walter, D. Jacobs, T. Duong, J. Peng, L. Jiang, Y.-B. Cheng and K. Weber, *Adv. Funct.Mater.*, 2016, **26**, 6807-6813.

3 H. Zhou, Q. Chen, G. Li, S. Luo, T.-b. Song, H.-S. Duan, Z. Hong, J. You, Y. Liu and Y. Yang, *Science*, 2014, **345**, 542-546.

4 D. Luo, L. Zhao, J. Wu, Q. Hu, Y. Zhang, Z. Xu, Y. Liu, T. Liu, K. Chen, W. Yang, W. Zhang, R. Zhu and Q. Gong, *Adv. Mater.*, 2017, **29**, 1604758.

5 D. Shi, V. Adinolfi, R. Comin, M. Yuan, E. Alarousu, A. Buin, Y. Chen, S. Hoogland, A. Rothenberger and K. Katsiev, *Science*, 2015, **347**, 519-522.

6 D.-Y. Son, J.-W. Lee, Y. J. Choi, I.-H. Jang, S. Lee, P. J. Yoo, H. Shin, N. Ahn, M. Choi and D. Kim, *Nature Energy*, 2016, **1**, 16081.

7 W. S. Yang, J. H. Noh, N. J. Jeon, Y. C. Kim, S. Ryu, J. Seo and S. I. Seok, *Science*, 2015, **348**, 1234-1237.

8 H. Tan, A. Jain, O. Voznyy, X. Lan, F. P. G. de Arquer, J. Z. Fan, R. Quintero-Bermudez, M. Yuan, B. Zhang and Y. Zhao, *Science*, 2017, **355**, 722-726.

9 S. S. Shin, E. J. Yeom, W. S. Yang, S. Hur, M. G. Kim, J. Im, J. Seo, J. H. Noh and S. I. Seok, *Science*, 2017, **356**, 167-171.

10 M. Saliba, T. Matsui, K. Domanski, J.-Y. Seo, A. Ummadisingu, S. M. Zakeeruddin, J.-P. Correa-Baena, W. R. Tress, A. Abate and A. Hagfeldt, *Science*, 2016, **354**, 206-209.

11 X. Li, D. Bi, C. Yi, J. D. Decoppet, J. Luo, S. M. Zakeeruddin, A. Hagfeldt and M. Gratzel, *Science*, 2016, **353**, 58-62.

12 Q. Jiang, L. Zhang, H. Wang, X. Yang, J. Meng, H. Liu, Z. Yin, J. Wu, X. Zhang and J. You, *Nature Energy*, 2016, **2**, 16177.

13 M. Zhang, J. S. Yun, Q. Ma, J. Zheng, C. F. J. Lau, X. Deng, J. Kim, D. Kim, J. Seidel, M. A. Green, S. Huang and A. W. Y. Ho-Baillie, *ACS Energy Lett.*, 2017, **2**, 438-444.

14 E. H. Anaraki, A. Kermanpur, L. Steier, K. Domanski, T. Matsui, W. Tress, M. Saliba, A. Abate, M. Grätzel and A. Hagfeldt, J. P. Correa-Baena, *Energy Environ. Sci.*, 2016, **9**, 3128-3134.

15 T. Ye, S. Ma, X. Jiang, L. Wei, C. Vijila and S. Ramakrishna, *Adv. Funct.Mater.*, 2017, 1606545, DOI: 10.1002/adfm.201606545.

16 D. Bi, W. Tress, M. I. Dar, P. Gao, J. Luo, C. Renevier, K. Schenk, A. Abate, F. Giordano, J. P. Correa Baena, J. D. Decoppet, S. M. Zakeeruddin, M. K. Nazeeruddin, M. Gratzel and A. Hagfeldt, *Sci. Adv*, 2016, **2**, e1501170.

17 B. Ding, Y. Li, S.-Y. Huang, Q.-Q. Chu, C.-X. Li, C.-J. Li and G.-J. Yang, *J. Mater. Chem. A*, 2017, **5**, 6840-6848.

18 C. Momblona, L. Gil-Escrig, E. Bandiello, E. M. Hutter, M. Sessolo, K. Lederer, J. Blochwitz-Nimoth and H. J. Bolink, *Energy Environ. Sci.*, 2016, **9**, 3456-3463.

19 D. Bi, C. Yi, J. Luo, J.-D. Décoppet, F. Zhang, S. M. Zakeeruddin, X. Li, A. Hagfeldt and M. Grätzel, *Nature Energy*, 2016, **1**, 16142.

20 M. Saliba, T. Matsui, J.-Y. Seo, K. Domanski, J.-P. Correa-Baena, M. K. Nazeeruddin, S. M. Zakeeruddin, W. Tress, A. Abate, A. Hagfeldt and M. Gratzel, *Energy Environ. Sci.*, 2016, **9**, 1989-1997.

21 F. Cai, L. Yang, Y. Yan, J. Zhang, F. Qin, D. Liu, Y.-b. Cheng, Y. Zhou and T. Wang, *J. Mater. Chem. A*, 2017, DOI:10.1039/C7TA02317K.